Near-infrared–terahertz hyper-Raman spectroscopy of an excited silicon surface

L. Dalstein, M. Tondusson, M. Kristensen, E. Abraham, J. Degert, Eric Freysz

Near-infrared - Terahertz hyper-Raman spectroscopy of an excited silicon surface

L. Dalstein,[1] M. Tondusson,[1] M.H. Kristensen,[1] E. Abraham,[1] J. Degert,[1] and E. Freysz[1]
CNRS, LOMA UMR 5798, University Bordeaux, 33405 Talence, France

(*Electronic mail: eric.freysz@u-bordeaux.fr)

(Dated: 17 October 2024)

We recorded the hyper-Raman spectra resulting from the interaction of a near-infrared (near-IR) picosecond pulse and a terahertz (THz) ultrashort pulse at the surface of a (111) silicon sample. A simple model is proposed to analyze the evolution of the hyper-Raman spectra vs the time delay between the near-IR and THz pulses. It links the hyper-Raman spectra to the multi-phonon absorption in silicon. This approach makes it possible to demonstrate that, during carrier generation by the near-IR pulse, the two-phonon and three-phonon absorption bands are enhanced in modes involving optical phonons. This process results from the very rapid and strong population of the optical phonons induced by the photo-generated hot carriers. It occurs over a few hundreds of femtoseconds and lasts throughout the duration of the near-IR pulse.

I. INTRODUCTION

Second-harmonic generation (SHG) has been established as a powerful and versatile technique for characterizing the surface and interface of materials.[1,2] In centrosymmetric materials, second-order nonlinear processes are forbidden in the bulk but occur at the surface, where the inversion symmetry is broken. This highly sensitive technique has been widely used to characterize silicon interfaces, which play an important role in many electronic devices.[3–11] SHG can also be recorded in a centrosymmetric material when a static field is applied.[12–15] The phenomenon can also be used to measure rapidly varying electric fields guided by transmission lines[16,17] or freely propagating terahertz (THz) pulses.[18] This latter technique, known as THz field induced second-harmonic (TFISH), has been used to characterize buried silicon interfaces or crystalline silicon.[19,20] The development of intense and broadband THz sources has given rise to the topical field of "THz nonlinear optics". TFISH belongs to this field, but many other processes, including the THz induced Kerr effect[21], THz sum-frequency excitation of a Raman-active mode,[22] and coherent THz hyper-Raman scattering[23–25] have also been reported.

At the surface of silicon, different processes have been identified to account for TFISH.[19,20,26] However, the acronym TFISH may be misleading. In this process, the generated field writes $E_{\mathrm{TFISH}}(2\omega\pm\Omega)\propto\chi^3(\omega,\omega,\Omega,2\omega\pm\Omega)E^{(*)}(\Omega)E^2(\omega)$, where $E^{(*)}(\Omega)$ is the THz electric field or its complex conjugate, $E(\omega)$ is the near-IR electric field and $\chi^3(\omega,\omega,\Omega,2\omega\pm\Omega)$ is the third-order nonlinear optical susceptibility of the material. This expression shows TFISH is not actually a SHG process but rather a hyper-Raman scattering (HRS) process leading to the generation, in the bulk of the material, of Stokes $(2\omega-\Omega)$ and anti-Stokes $(2\omega+\Omega)$ frequency components around 2ω. This process is strongly enhanced when one of the frequencies in the nonlinear susceptibility $\chi^3(\omega,\omega,\Omega,2\omega\pm\Omega)$, such as Ω, is resonant with the material.[2] Thus, the enhancement of the HRS signal at a frequency of $2\omega\pm\Omega_1$ is the signature of a resonant infrared (IR) active mode of the material at Ω_1. In the following, we use this process to reveal the significant increase in the two-phonon absorption and the enhancement of three-phonon absorption involving optical phonons, as well as their evolution during the photoexcitation of Si(111) by a near-IR pulse.

II. EXPERIMENTAL SETUP

Our experiment setup, sketched in Fig. 1, is built around a 3.5 mJ Ti:Sapphire regenerative amplifier laser system. This laser system operates at a 1 kHz repetition rate, delivering 50 fs pulses centered around 800 nm, which are split into two beams. In the first beam, a 1 mJ pulse is used to generate ultrashort THz pulse from two-color femtosecond laser-induced filamentation in air.[27,28] This method involves focusing intense femtosecond laser pulses into a gas medium (typically air) to form a plasma, which in turn generates THz radiation. When the fundamental (800 nm) and the second harmonic (400 nm) overlap temporally and spatially in the filament, their superposition creates an asymmetric electric field. This field accelerates the free electrons in the plasma non-symmetrically, inducing a time-varying current. This rapidly varying plasma current is responsible for emitting broadband THz radiation. The generated THz pulse is transmitted through a 1 mm high-resistivity float zone (HRFZ) silicon wafer set at the THz Brewster angle to minimize the absorption and reflection losses and filter out the remaining near-IR beam. It is then collimated and focused onto the crystalline silicon sample (Siltronic, intrinsic, R> 200 Ω.cm) using two off-axis parabolic mirrors (PMs). The second beam is filtered by a zero dispersion line in the center of which a narrow slit is inserted. This system makes it possible to generate a synchronized narrow band ($\Delta\lambda\sim20\,\mathrm{cm}^{-1}$) near-IR pulse centered at 800 nm whose duration at full width half maximum (FWHM) is $\tau\approx500$ fs. The energy of this pulse is adjusted to ~2 µJ using a zero order half wave plate and a polarizing beam splitter. It is then focused (beam waist of ~50 µm) onto the silicon sample through a hole in the PM

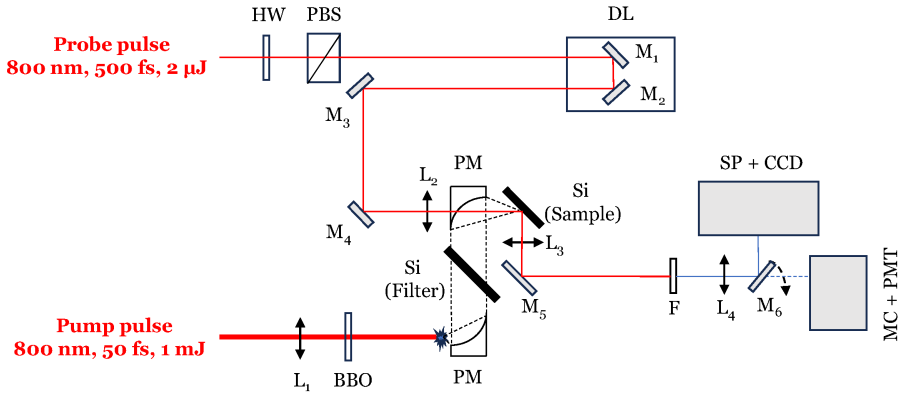

FIG. 1. Experimental setup. HW: zero-order half-wave plate, PBS: polarizing beam splitter, DL: optical delay line, $M_{1,\ldots,6}$: high reflection and low dispersion mirror, $L_{1,\ldots,4}$: lens, BBO: beta barium borate SHG crystal, PM: off-axis parabolic mirror, Si: high resistivity silicon wafer, F: IR filter, MC+PMT: monochromator connected to a photomultiplier tube, and SP + CCD: spectrometer coupled to a thermally cooled charged coupled device. The mirror M_6 can be flipped to switch from one detector to the other.

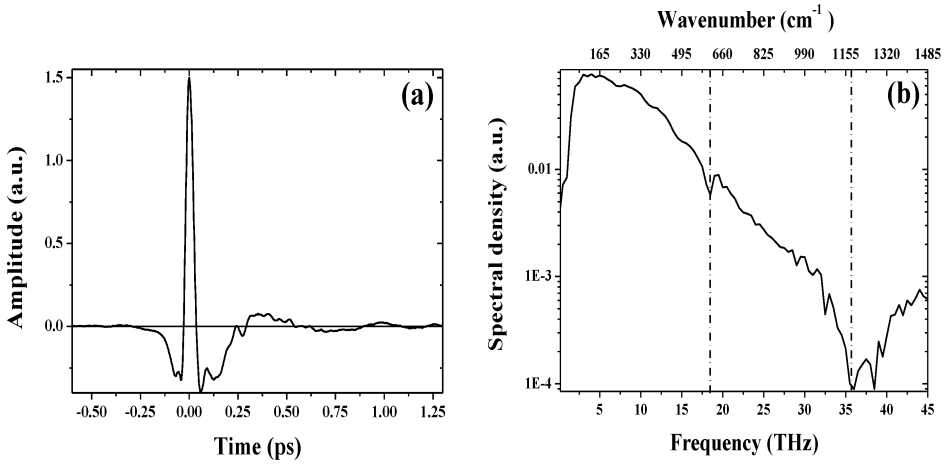

FIG. 2. Temporal evolution of the generated THz pulse (a) and its spectrum (b) after transmission by the HRFZ silicon wafer.

using a lens with a focal length of f =125 mm. The collinear THz and near-IR pulses are incident on the silicon sample at an angle of 45° . The THz and near-IR pulses are respectively p- and s-polarized. Finally a motorized translation stage enables precise control of the time delay between the two pulses. The HRS signal generated in the bulk near the surface of the silicon sample is collimated and detected by either a photomultiplier tube (PMT) positioned at the exit of a monochromator (MC) or a spectrometer connected to a thermally cooled charge device (CCD) camera. To record the evolution of the HRS signal the THz pulse is chopped at 500 Hz. A lock-in amplifier enables us to subtract the surface SHG from the recorded signal, leaving us with a pure HRS signal.

III. EXPERIMENTAL RESULTS

First, we characterized the THz pulse at the sample position using an air biased coherent detection device (ZAP-APD from DHC).[29] The THz waveform and its spectrum are displayed in Fig. 2. This very short THz pulse (∼60 fs at FWHM) exhibits a very broad spectrum centered at ∼5 THz, extending up to 45 THz. The spectrum reveals two distinct absorption bands at ∼35.4 THz (∼1160 cm^{-1}) and ∼18.5 THz (∼610 cm^{-1}). They most likely correspond to absorption of impurities of interstitial oxygen[30] and two-phonon absorption in the thick silicon wafer, respectively. While the absorption of a photon with energy below the band gap is forbidden in silicon due to its diamond-like structure, it may occur through the excitation of two phonons whose sum or difference in energies equals the photon energy.[31,32]

Next, the pure HRS signal generated in the Si(111) sample was recorded as a function of the delay Δt using the PMT. Its

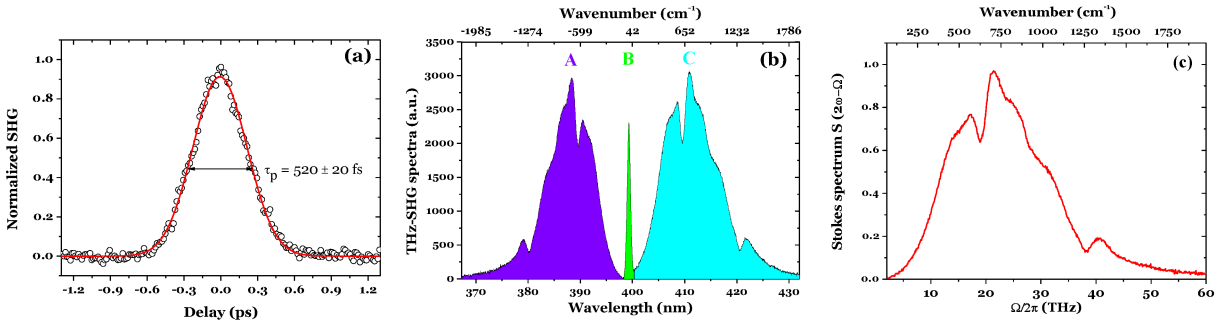

FIG. 3. a) Temporal evolution of the SHG signal recorded by the photomultiplier. b) Spectrum of the SHG signal recorded by the CCD camera at the zero delay. c) Normalized Stokes spectrum vs the frequency shift.

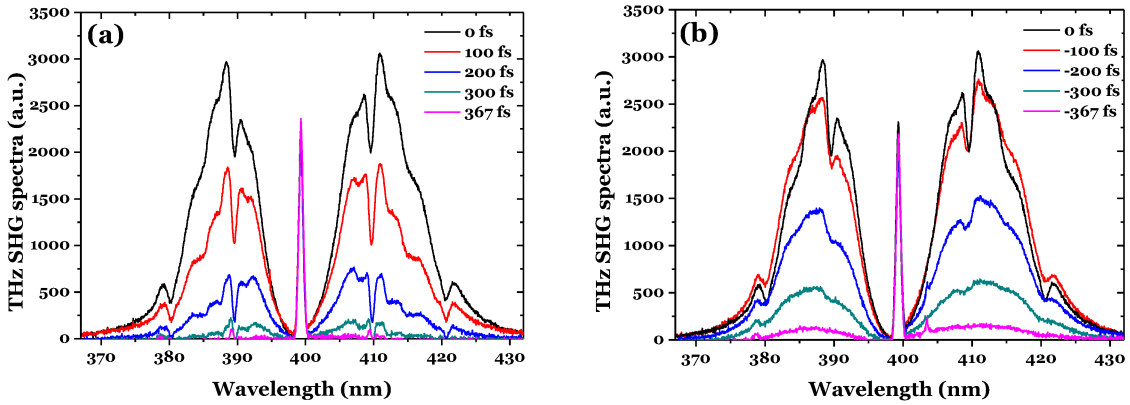

FIG. 4. Temporal evolution of the HRS spectra. a) HRS spectra for $\Delta t > 0$ when the THz pulse is ahead of the near-IR pulse. b) HRS spectra for $\Delta t < 0$ when the near-IR pulse is ahead of the THz pulse.

temporal evolution is shown in Fig. 3a. It is well fitted by a Gaussian function with a FWHM of 520±20 fs, close to the FWHM of the near-IR pulse.

Subsequently, the HRS signal was recorded at the zero-delay ($\Delta t = 0$). The latter which includes the surface SHG is displayed in Fig. 3b. The spectrum highlights three distinct spectral regions. The narrow central peak, labeled B, is centered at half the wavelength of the near-IR pulse with a spectral width of $\sim$20 cm^{-1}. It persists even when the THz pulse is blocked, indicating its link to surface SHG. The broadband spectral features, labeled A and C, are almost mirrored across the SHG peak. Their maxima are shifted by roughly $\pm$21 THz ($\pm$11 nm) compared to the SHG peak. They disappear when either the near-IR or THz pulse is blocked. Two marked dips appear in each side bands, offset by about $\pm$18.5 THz ($\pm$10 nm or $\pm$625 cm^{-1}) and $\pm$37 THz ($\pm$20 nm or $\pm$1250 cm^{-1}) from the SHG maximum. These dips correspond to those exhibited by the THz spectrum [Fig. 2b] due to the absorption of the filter. The temporal evolution of the entire spectrum, allows us to infer that a four-wave mixing is giving rise to the HRS signal. The normalized Stokes spectrum, ranging from 402 to 435 nm, is presented in Fig.3c. The temporal evolution of the entire signal (HRS +SHG) is displayed in Fig. 4. We notice that the amplitude of the narrow SHG peak remains almost constant, while the A and C side bands change drastically in terms of shape and amplitude, but remain mirrored across the SHG peak. As shown in Fig. 4a, when the THz pulse is ahead ($\Delta t > 0$) of the near-IR pulse, the side band amplitudes decrease rapidly. However, the dips at $\sim$18.5 and $\sim$37 THz remain clearly visible. This is notably different in Fig. 4b, where the near-IR pulse is ahead of the THz pulse ($\Delta t < 0$). The side band amplitudes are in this case larger and the two dips at $\sim$18.5 THz and $\sim$37 THz are significantly broadened.

The temporal asymmetry of the (anti-)Stokes amplitudes is clearly evident from Fig. 5, where the Stokes signal $S(2\omega - \Omega_1, \Delta t)$ at 415 nm ($\Omega_1 = 27$ THz) has been extracted. That is, the signal envelope is slightly asymmetric, with a maximum delay of $\sim$50 $\pm$ 20 fs..

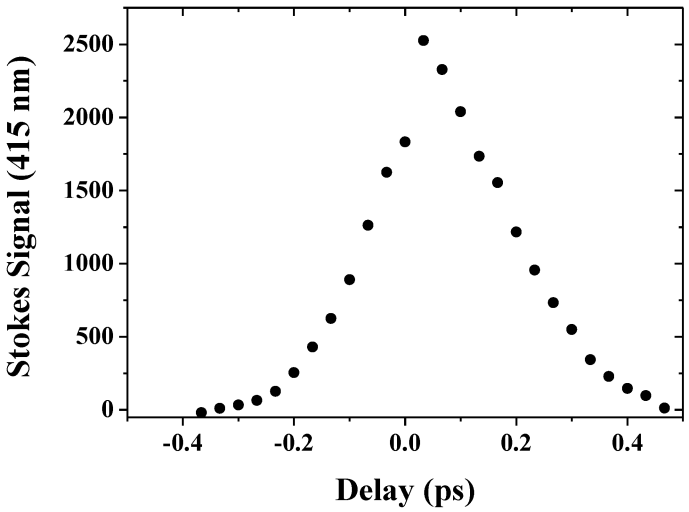

FIG. 5. Evolution of the amplitude of the Stokes spectral component centered at 415 *nm* vs the delay between the near-IR and THz pulses

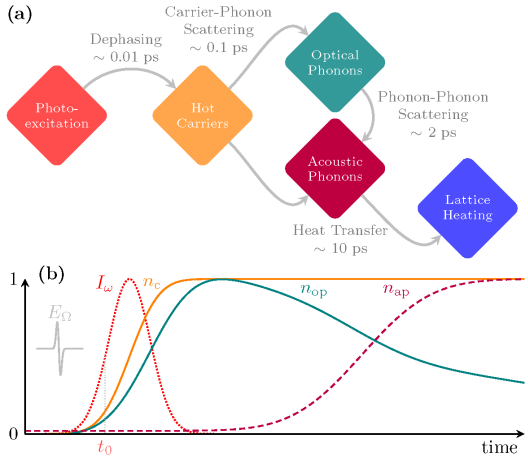

FIG. 6. (a) Illustration of the mechanisms in play and the relevant time scales. (b) Time evolution of pertinent quantities. Namely, the near-IR pulse I_ω, the number of carriers n_c, optical phonons n_{op}, and acoustic phonons n_{ap}.

IV. THE MECHANISM IN PLAY

Before addressing the theoretical description of the phenomenon we recorded, we will discuss the physical mechanisms accounting for the temporal evolution of the hyper-Raman spectra. These mechanisms, illustrated in Fig. 6, result from the absorption of the near-IR pulse in the sample. The near-IR photon energies are above the silicon band gap. At time t_0, the intensity of the Gaussian near-IR pulse I_ω is sufficiently large to highly excite carriers (i.e. electrons and holes) far above and below the conduction and valence band edges, respectively. Initially, these carriers are correlated. However, due to carrier-carrier scattering, they quickly dephase after a few tens of femtoseconds. This process results in a high-density non-equilibrium distribution of very hot carriers (HCs) at the surface silicon sample, over a thickness of $L_{\text{abs}} \sim 1\,\mu$m. The HCs rapidly transfer their excess energy within a few hundreds of femtoseconds through carrier-carrier scattering and/or interactions with optical phonons (OPs). Thereby, the HCs thereby thermalize and form a quasi-equilibrium Fermi-Dirac distribution . Meanwhile, carriers are continuously photoexcited throughout the duration of the near-IR pulse. The above-described HCs are particularly excited during the full width half maximum (FWHM) duration τ_p. The temporal evolution of the carrier population can be expressed as

$$n_c(t) \propto n_0 + \frac{n_g}{2}[1 + \text{erf}(t/\tau_p)], \tag{1}$$

where erf() denotes the error function and $n_0 \sim 10^{11}$ per cm^3 is the initial and very low carrier density in our sample. Considering that in our experiment 60% of the near-IR pulse energy is absorbed by silicon and that each photon creates an electron hole-pair, the 2 μJ pulse creates $n_g \sim 6\ 10^{21}$ carriers per cm^3 within its interaction volume. The ongoing excitation of non-equilibrium HCs leads to an ever-increasing and out-of-equilibrium population of hot OPs. Hence, the population of OPs n_{op} rapidly increases, and because the carriers are already highly excited, the remaining hot OPs cannot easily relax. After roughly 2 ps,[33] the abundance of OPs scatters with the few acoustic phonons (APs) present at room temperature. This allows the OP population to decay, while the AP population n_{ap} increases, and in turn, permits the HCs to decay to equilibrium. Finally, a THz pulse delayed with respect to the near-IR pulse is shined on the sample. Since the THz pulse is much shorter ($\sim$60 fs) than the near-IR pulse, one can consider that the experiment reveals the evolution of the far-IR absorption (i.e. the Stokes or anti-Stokes bands) in the sample during the near-IR pulse. Moreover, the measured far-IR spectra are primarily limited in resolution by the spectral width of the near-IR pulse (i.e. ~ 20 cm^{-1}).

Another important parameter to evaluate, is the thickness of the layer contributing to the spectra displayed in Fig. 3 and 4. As mentioned, the narrow SHG peak at 400 nm results from the top atom layer of the silicon sample,[3] while the broad side bands are linked to the HRS taking place in the bulk. The thickness over which these later spectral components are generated in reflection is about the coherence length $L_{\text{coh}} \sim 1/\Delta k(2\omega \pm \Omega)$, where

$$\Delta k(2\omega \pm \Omega) = k(2\omega \pm \Omega) + 2k(\omega) \pm k(\Omega) = \frac{2\omega \pm \Omega}{c} n(2\omega \pm \Omega) + \frac{2\omega}{c} n(\omega) \pm \frac{\Omega}{c} n(\Omega). \tag{2}$$

Since $\Omega \ll \omega$ and $n(\Omega) \approx n(\omega) \approx n(2\omega \pm \Omega)$ for silicon, the coherence length $L_{\text{coh}} \sim c/4\omega n(\omega) = \lambda/8\pi n(\lambda)$. Here, $n(\lambda)$ is the refractive index at wavelength λ. The refractive index of silicon is $n(\lambda) \approx 4$ at the central wavelength of the near-IR pulse ($\lambda = 800$ nm). Thus, the coherence length for the HRS process is $L_{\text{coh}} \sim 8$ nm. This interaction length is very small compared to the typical absorption length of THz and near-IR waves (≥ 1 µm). We will therefore consider that the amplitude of the near-IR and THz fields remains almost constant over L_{coh} in our experiment.

V. A SIMPLE MODEL

The interaction between the near-IR and THz pulses, centered at the ω and Ω frequencies, respectively, generates different nonlinear polarization terms in the bulk and at the surface of the silicon. Hereafter, we will only retain the spectral components of the nonlinear polarization relevant to describe our experimental results.

The first term results from the interaction of the near-IR pulse with the silicon. It is written as follows:

$$P_i^{(2)}(2\omega) = \chi_{ijk}^{(2)}(2\omega) E_j(\omega) E_k(\omega) + \text{c.c.} \quad , \tag{3}$$

where $E_{j,k}(\omega)$ are the components of the near-IR electric field, $\chi_{ijk}^{(2)}(2\omega)$ are the components of the second-order susceptibility tensor, and c.c. is the complex conjugate of the previous expression. We will consider that the second-order susceptibility tensor does not depend on the different spectral components within the near-IR field. Since silicon is a centrosymmetric material, this nonlinear polarization is only generated at the surface itself, and the $\chi_{ijk}^{(2)}$ tensor components reflect the sample surface symmetry.[3]

The second term results from the mixing of the near-IR and THz pulses in the silicon sample. It gives rise to the Stokes (C band) and anti-Stokes (A band) spectral components. It is written as follows:

$$P_i^{(3)}(2\omega - \Omega, \Delta t) = \chi_{ijkl}^{(3)}(2\omega - \Omega, \Delta t) E_j(\omega) E_k(\omega) E_l^*(\Omega) e^{-\mathrm{i}\Omega\Delta t} + \text{c.c.} \quad : \text{ C band}, \tag{4}$$

$$P_i^{(3)}(2\omega + \Omega, \Delta t) = \chi_{ijkl}^{(3)}(2\omega + \Omega, \Delta t) E_j(\omega) E_k(\omega) E_l(\Omega) e^{\mathrm{i}\Omega\Delta t} + \text{c.c.} \quad : \text{ A band}. \tag{5}$$

where $E^*(\Omega)$ is the complex conjugate of the THz field, $\chi_{ijkl}^{(3)}(2\omega \pm \Omega, \Delta t)$ are the components of the effective third-order susceptibility tensor, and Δt is the time delay. These polarization components are generated over the coherence length L_{coh}, starting from the surface. The crystal symmetry rules make it possible to infer the different non-null components of $\chi_{ijkl}^{(3)}$. The effective third-order nonlinear susceptibility $\chi^{(3)}$ can be decomposed into a resonant and a non-resonant term

$$\chi^{(3)} = \chi_{\text{R}}^{(3)} + \chi_{\text{NR}}^{(3)} \tag{6}$$

We will consider that the non-resonant contribution does not depend on the time delay Δt nor the near-IR and THz frequency components. To account for the evolution of the phonon population upon creation of photocarriers in the sample by the near-IR pulse, we will assume that the resonant contribution mainly depends on the THz frequencies and the delay Δt:

$$\chi_{\text{R}}^{(3)}(2\omega \pm \Omega, \Delta t) = \sum_j \frac{C_j(\Delta t)}{\Omega^2 - \Omega_j^2 - 2\mathrm{i}\gamma_j(\Delta t)\Omega} \tag{7}$$

Here Ω_j is the pulsation of the resonance mode j, C_j is its amplitude, and γ_j is its damping constant. We introduce $C_j(\Delta t)$ and $\gamma_j(\Delta t)$ to account for the frequency change in both optical and acoustic phonons induced by the photo-generated carriers and lattice softening in silicon.[34]

These nonlinear polarizations will radiate electric fields oscillating at the 2ω and $2\omega \pm \Omega$ frequencies. The radiated fields write:

$$\frac{\partial E_j(2\omega,z)}{\partial z} = \mathrm{i}\frac{2\omega}{c} P_j^{(2)}(2\omega,z) \ , \tag{8}$$

$$\frac{\partial E_j(2\omega\pm\Omega,\Delta t)}{\partial z} = \mathrm{i}\frac{2\omega\pm\Omega}{c} P_j^{(3)}(2\omega\pm\Omega,\Delta t) \ . \tag{9}$$

When integrated over the coherence length L_{coh}, the spectral density of the HRS signal $S(2\omega\pm\Omega,\Delta t)$ is proportional to $|L_c \sum_j P_j^{(3)}(2\omega\pm\Omega,\Delta t)|^2$. Hereafter, we will consider that in our experiment we are always very close to a phonon resonance so that $\chi^{(3)}$ is imaginary and negative.

VI. DISCUSSION

The crystal symmetry group ($m3m$) implies that one should not expect any interaction between a single phonon and THz radiation in perfect silicon. However, impurities and structure defects can introduce such THz absorption. In addition, the simultaneous interaction of two, three, or four phonons can also produce an electric dipole moment with which IR radiation can interact. These have been shown to result in absorption ranging from 9 THz ($\sim$300 cm^{-1}) up to 57 THz ($\sim$1900 cm^{-1}).[35,36] Since the highest phonon energy in silicon is 15.7 THz ($\sim$520 cm^{-1})[32] we will assign the very low tail absorption ranging from 60.7 THz ($\sim$2000 cm^{-1}) to 45.4 THz ($\sim$1500 cm^{-1}) to four-phonon absorption, the weak band between 45.4 THz ($\sim$1500 cm^{-1}) down to 30.3 THz ($\sim$1000 cm^{-1}) to three-phonon absorption, and the main band below 30.3 THz ($\sim$1000 cm^{-1}) to a two-phonon absorption.

In the latter case, selection rules dictates that the two phonons must be of distinct branches of the vibration spectrum. They can either have opposite or equal momenta, giving rise to the so-called summation and difference bands, respectively. The summation band originates from two phonons being simultaneously emitted or absorbed, while the difference band emerge from one being absorbed and another being created.[31] The two-phonon absorption resulting from the summation, $\alpha(\Omega_1+\Omega_2)$, and the difference, $\alpha(\Omega_1-\Omega_2)$ bands scale as $[(n(\Omega_1)+1)(n(\Omega_2)+1)-n(\Omega_1)n(\Omega_2)]$ and $[n(\Omega_1)(n(\Omega_2)+1)-n(\Omega_2)(n(\Omega_1)+1)]$, respectively. Here $n(\Omega)$ is the occupation number of a phonon mode whose pulsation is Ω. At thermal equilibrium it writes $n(\Omega)=[\exp(\hbar\Omega/k_\mathrm{B}T)-1]^{-1}$ where T, $\hbar$ and k_B are the temperature and the reduced Planck and Boltzmann constants, respectively.

TABLE I. Assignment of multi-phonon absorption peaks in silicon.[32,35]

ν (cm^{-1})	$\Omega/2\pi$ (THz)	Amplitude	Width (cm^{-1})	Suggested assignment
493	14.9	0.6	20	LA+TA
566	17.1	0.2	6	LO+TA
610	18.5	0.47	2.5	TO+TA
740	22.4	0.6	12	LO+LA
819	24.8	0.4	13	TO+LA
896	27.1	0.5	13	TO+LO
964	29.2	0.4	13	TO+TO
1100	33.3	0.5	15	interstitial oxygen mode
1302	39.4	0.2	12.5	TO+LO+LO
1380	41.8	0.2	12.5	TO+TO+LO
1450	43.9	0.2	12.5	TO+TO+TO

As mentioned, the energy of the photoexcited carriers in silicon is mainly transferred to OPs, which have higher energy. Upon photoexcitation by a picosecond near-IR pulse, the generation rate of the OPs greatly exceeds their decay rate, giving rise to an out of equilibrium OP population that subsequently transfers their energy to APs. After excitation, the carrier-OP coupling process continues until the excess energy of the HCs is less than the OP energies. Then, OPs decay into APs. Thus, all multi-phonon processes involving OPs are rapidly enhanced within less than 100 fs after excitation. During the photoexcitation, the amplitude of three- or even four-phonon processes involving OPs is expected to be substantially increased compared to the two-phonon processes involving an AP. Furthermore, it must be kept in mind that the photocarrier generation also results in a shift and non-negligible broadening of the phonon modes.[34]

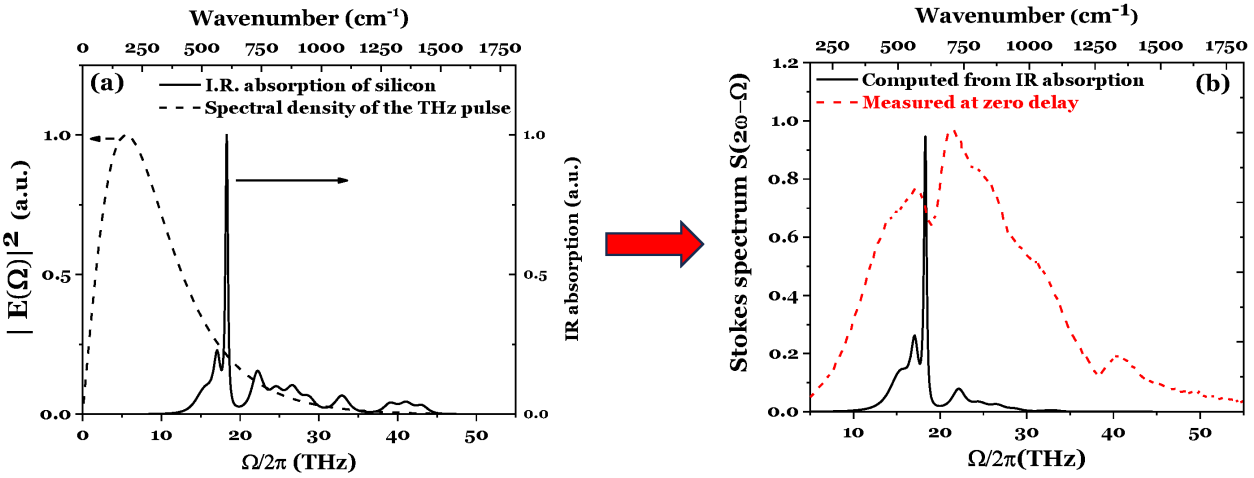

FIG. 7. a) Computed IR absorption of silicon at room temperature and THz pulse and spectral density of the THz field distribution (normalized to unity). b) In the solid black line is the computed hyper-Raman Stokes spectrum of silicon at room temperature (normalized to unity). In the red dashed line, the experimental hyper-Raman Stokes spectrum previously displayed in Fig.3c.

Figure 7b displays the computed Stokes spectrum (black line) that should be recorded at the very early stage of photo-excitation. That is, when density of generated photocarriers in silicon is so low that its IR absorption is comparable to the room temperature value. First, we computed the far-IR absorption of silicon at room temperature (Fig. 7a), which evolves like $|\mathrm{Im}(\chi_R^{(3)}(2\omega \pm \Omega))|$, where Im denotes the imaginary part. This spectrum was calculated by considering different Lorentzian contributions as specified in Table I.[35] We neglected the weaker IR absorptions occurring at lower frequencies ($\Omega/2\pi < 10$ THz) resulting from difference absorption processes.[36] Notably, the two-phonon absorptions ranging from 14.9 THz ($\sim$493 cm^{-1}) to 24.8 THz ($\sim$819 cm^{-1}) results from the combination of an AP and OP, whereas those in between 27.1 THz ($\sim$896 cm^{-1}) to 33.3 THz ($\sim$1100 cm^{-1}) are due to the combination of two OPs. Above 33.3 THz (1300 cm^{-1}), the three-phonon absorptions is associated with the combination of three OPs. By adjusting these parameters, we were able to closely reproduce the previously published IR absorption of silicon.[35]

Figure 7b displays the computed Stokes spectrum (black line) that should be recorded at the very early stage of photoexcitation. That is, when the density of generated photocarriers in silicon is comparable to the room temperature value. According to Eq. (9), one can calculate the Stokes and anti-Stokes spectra upon generation of photocarriers. In Figure 7, we have also plotted the Stokes spectrum recorded at zero delay (red dashed line) from Fig. 3c. A strong discrepancy is seen between the computed and measured spectra. This clearly evidences that the far-IR absorption of silicon is significantly modified during its photoexcitation by the near-IR pulse.

Similarly, we can obtain the evolution of the far-IR absorption $|\mathrm{Im}(\chi_R^{(3)}(2\omega \pm \Omega, \Delta t)|$ from our recorded (anti-)Stokes spectra $S(2\omega \pm \Omega)$ [Fig. 3b] by deconvolution with the experimental THz spectrum (Fig. 2b). That is,$|\mathrm{Im}(\chi_R^{(3)}(2\omega \pm \Omega, \Delta t))| \propto \sqrt{S(2\omega - \Omega)/|E(\Omega)|^2}$. The resulting Stokes spectra are shown in Fig.8a-b along with our model for unexcited silicon at room temperature [Fig.8c] Hereinafter, we will mainly focus on the spectral feature of $|\mathrm{Im}(\chi_R^{(3)}(2\omega \pm \Omega, \Delta t)|$ ranging from 5 to 50 THz, where the signal-to-noise ratio is large enough to conduct a meaningful discussion. In Fig. 8c, the dotted lines indicate the frequency ranges where the far-IR absorption results from the combination of an optical and an acoustic phonon (AP+OP), two optical phonons (OP+OP) and three optical phonons (OP+OP+OP).

When comparing Fig. 8(a) and 8(b) with Fig.8(c) many interesting features emerge. In the two-phonon band up to 25 THz, the main peak around 19 THz almost disappears, indicating a significant broadening of the related phonon modes. The features between 25 and 35 THz, resulting from two OPs (TO+LO, TO+TO), are enhanced compared to those below 25 THz involving AP modes (LO+TA, TO+TA, LO+LA, TO+LA). In the three-phonon band between 35 and 50 THz, $|\mathrm{Im}(\chi_R^{(3)}(2\omega - \Omega, \Delta t))|$ is significantly increased below 40 THz. The shift of the three-phonon absorption towards lower frequencies is likely related to the shift of the individual phonon modes upon photocarriers generation.[34] In Fig. 8a-b, the peak around 39 THz is close to the absorption resulting from the 2LO+TO modes. This peak is larger compared to the broad peak around 43 THz (2TO+LO,3TO). This may indicate that the LO phonon mode is more strongly populated than the TO phonon mode during the photogeneration of carriers.

These features do not drastically change with the delay Δt between the near-IR and THz pulse. A noticeable change vs Δt is the amplitude of the two-phonon absorption band compared to the three-phonon absorption band. When the THz pulse

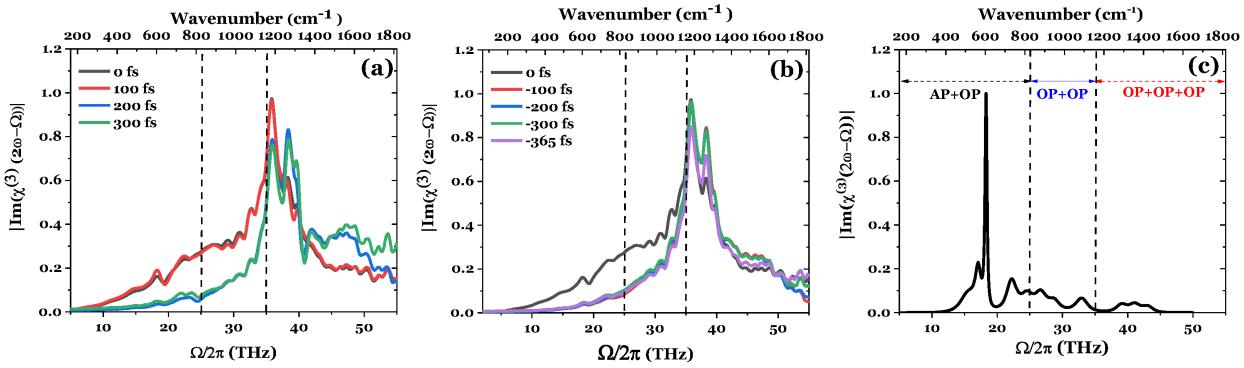

FIG. 8. (a) and (b) Evolution of $|\mathrm{Im}(\chi_R^{(3)}(2\omega-\Omega,\Delta t))|$ normalized to unity vs the delay between the near-IR and THz pulse. c) Computed spectrum of $|\mathrm{Im}(\chi_R^{(3)}(2\omega-\Omega))|$ for unexcited silicon at room temperature. The dotted lines separate the two-phonon absorption resulting from the combination of acoustic and optical phonons (AP+OP), from the two-phonon and three-phonon absorption resulting from the combination of two optical phonons (OP+OP) and three optical phonons (OP+OP+OP), respectively.

precedes the near-IR pulse ($\Delta t > 0$), the two-phonon absorption band is weaker than the three-phonon band. Then, it increases and reaches a maximum when the near-IR and THz pulses are perfectly overlapped ($\Delta t = 0$). Afterwards, it rapidly decreases. This behavior may be related to the rate at which we populate the OP modes. When the THz pulse precedes the near-IR pulse, this rate decreases. It reaches its maximum when $\Delta t = 0$. Afterwards, it steadily decreases. This could indicate that when the generation rate of OPs is very high, the two-phonon absorption becomes stronger. The phenomenon likely depends on the density of photogenerated carriers.

The asymmetry displayed in the Fig. 5 is not surprising, as the photogenerated HCs need ∼400 fs before emitting an OP through their interaction with the lattice.[37] This depends on the density of photogenerated carriers[33]. While Fig.5 also reveals the kinetics of the creation and relaxation of the LO phonon, its evolution is mainly driven by the temporal evolution of the near-IR intensity $I(\omega)$. Indeed, the latter is responsible for both the creation of the photocarriers, inducing a modification of $\chi^{(3)}(2\omega\pm\Omega,\Delta t)$, and the generation of the nonlinear polarization $P^{(3)}(2\omega\pm\Omega_1,\Delta t) \propto \chi^{(3)}(2\omega\pm\Omega,\Delta t)I(\omega,\Delta t)$. It is therefore very difficult to extract a meaningfully time constant for the LO phonon time constant.

So far, we have neglected the interference between $\chi^{(3)}$ and $\chi^{(2)}$ processes. We can evaluate this by examining the amplitude of the Stokes and anti-Stokes bands near the SHG peak (Fig. 3). Around this peak, the anti-Stokes component is almost null, while the Stokes can be clearly observed. Since the Stokes and anti-Stokes Raman susceptibities are related by $\chi_R^{(3)}(\omega_s) = \chi_R^{(3)*}(\omega_{as})$, it follows that $\mathrm{Im}(\chi_R^{(3)}(2\omega-\Omega)) = -\mathrm{Im}(\chi_R^{(3)}(2\omega+\Omega))$.[38] Therefore, we can conclude that the SHG peak should have approximately the same amplitude at both sides but interferes constructively with the Stokes field and destructively with the anti-Stokes field.

VII. CONCLUSION

We have reported on the HRS spectrum resulting from the interaction of a picosecond near-IR and an ultrashort THz pulse near the surface of a (111) silicon sample. These spectral contributions are large and very broad compared to the SHG signal purely generated by the near-IR picosecond pulse at the silicon surface. The HRS spectrum, whose amplitude depends on the temporal overlap between the near-IR and THz pulses, exhibits distinct dips related to two-phonon and interstitial oxygen absorption, which are broadened throughout the duration of the near-IR pulse. To account for the shape of the HRS spectrum and its temporal evolution, we proposed a simple model. It relates the HRS spectrum to multi-phonon absorption in silicon. Based on this model, we showed that during the generation of photocarriers by the near-IR pulse, the two- and three-phonon absorption bands are largely enhanced. Mainly towards the modes involving two or even three optical phonons. This process happens within ∼ 100 fs upon photoexcitation and results from the very rapid and strong population of optical phonons. This technique can easily be extended to study multi-phonons absorption in other crystals belonging to the $m3m$ symmetry group, such as diamond or germanium. While our current experimental setup limited the study of the hot phonon dynamics, it could easily be studied in a pump-probe experiment. This limitation can be easily circumvented by implementing a pump-probe setup. A short optical pump pulse should be used to populate the hot phonons in the sample. The temporal evolution of these hot phonons could then be probed using the approach described in this paper. It is worth noting that in this configuration, the temporal and spectral resolution will be limited by the duration of the picosecond pulse. The application of this technique to new superconductor,[39] topological insulator,[40] and 2D hetero-structures[41] will help improving our understanding of the electron-phonon interactions in

all these novel materials.

ACKNOWLEDGMENTS

We wish to acknowledge the support of the project Marie-Curie : 896908, SAInTHz, and the French State in the framework of the Investments for the Future programme IdEx University of Bordeaux.

[1] Y. R. Shen, "Surface studies by optical second harmonic generation: An overview," Journal of Vacuum Science & Technology B: Microelectronics Processing and Phenomena **3**, 1464–1466 (1985).
[2] Y. R. Shen, "Surface properties probed by second-harmonic and sum-frequency generation," Nature **337**, 519–525 (1989).
[3] H. W. K. Tom, T. F. Heinz, and Y. R. Shen, "Second-Harmonic Reflection from Silicon Surfaces and Its Relation to Structural Symmetry," Physical Review Letters **51**, 1983–1986 (1983).
[4] T. F. Heinz, M. M. T. Loy, and W. A. Thompson, "Study of Si(111) Surfaces by Optical Second-Harmonic Generation: Reconstruction and Surface Phase Transformation," Physical Review Letters **54**, 63–66 (1985).
[5] T. F. Heinz, M. M. T. Loy, and W. A. Thompson, "Study of symmetry and disordering of Si(111)-7×7 surfaces by optical second harmonic generation," Journal of Vacuum Science & Technology B: Microelectronics Processing and Phenomena **3**, 1467–1470 (1985).
[6] L. L. Kulyuk, D. A. Shutov, E. E. Strumban, and O. A. Aktsipetrov, "Second-harmonic generation by an $SiO_2 - Si$ interface: influence of the oxide layer," J. Opt. Soc. Am. B **8**, 1766–1769 (1991).
[7] Y. Qiang An and S. T. Cundiff, "Bulk and surface contributions to resonant second-harmonic generation from Si(001) surfaces," Applied Physics Letters **81**, 5174–5176 (2002).
[8] G. Lüpke, D. J. Bottomley, and H. M. Van Driel, "Second- and third-harmonic generation from cubic centrosymmetric crystals with vicinal faces: phenomenological theory and experiment," Journal of the Optical Society of America B **11**, 33 (1994).
[9] W. Daum, H.-J. Krause, U. Reichel, and H. Ibach, "Nonlinear optical spectroscopy at silicon interfaces," Physica Scripta **T49B**, 513–518 (1993).
[10] G. Erley and W. Daum, "Silicon interband transitions observed at $Si(100) - SiO_2$ interfaces," Physical Review B **58**, R1734–R1737 (1998).
[11] J. Sipe, D. Moss, and H. Van Driel, "Phenomenological theory of optical second- and third-harmonic generation from cubic centrosymmetric crystals," Physical Review B **35**, 1129–1141 (1987).
[12] R. W. Terhune, P. D. Maker, and C. M. Savage, "Optical Harmonic Generation in Calcite," Physical Review Letters **8**, 404–406 (1962).
[13] C. H. Lee, R. K. Chang, and N. Bloembergen, "Nonlinear Electroreflectance in Silicon and Silver," Physical Review Letters **18**, 167–170 (1967).
[14] P. Godefroy, W. De Jong, C. W. Van Hasselt, M. A. C. Devillers, and T. Rasing, "Electric field induced second harmonic generation spectroscopy on a metal-oxide-silicon structure," Applied Physics Letters **68**, 1981–1983 (1996).
[15] H. Guillet De Chatellus and E. Freysz, "Static and dynamic profile of the electric field within the bulk of fused silica glass during and after thermal poling," Optics Letters **28**, 1624 (2003).
[16] C. Ohlhoff, C. Meyer, G. Lüpke, T. Löffler, T. Pfeifer, H. G. Roskos, and H. Kurz, "Optical second-harmonic probe for silicon millimeter-wave circuits," Applied Physics Letters **68**, 1699–1701 (1996).
[17] A. Nahata, T. F. Heinz, and J. A. Misewich, "High-speed electrical sampling using optical second-harmonic generation," Applied Physics Letters **69**, 746–748 (1996).
[18] A. Nahata and T. F. Heinz, "Detection of freely propagating terahertz radiation by use of optical second-harmonic generation," Optics Letters **23**, 67 (1998).
[19] S. B. Bodrov, A. N. Stepanov, E. A. Burova, Y. A. Sergeev, A. I. Korytin, and M. I. Bakunov, "Terahertz-field-induced second harmonic generation for nonlinear optical detection of interfaces buried in transparent materials," Applied Physics Letters **119**, 221109 (2021).
[20] S. B. Bodrov, Y. A. Sergeev, A. I. Korytin, and A. N. Stepanov, "Terahertz-field-induced second optical harmonic generation from Si(111) surface," Physical Review B **105**, 035306 (2022).
[21] M. C. Hoffmann, N. C. Brandt, H. Y. Hwang, K.-L. Yeh, and K. A. Nelson, "Terahertz Kerr effect," Applied Physics Letters **95**, 231105 (2009).
[22] S. Maehrlein, A. Paarmann, M. Wolf, and T. Kampfrath, "Terahertz Sum-Frequency Excitation of a Raman-Active Phonon," Physical Review Letters **119**, 127402 (2017).
[23] S. Mou, A. Rubano, and D. Paparo, "Terahertz hyper-Raman time-domain spectroscopy of gallium selenide and its application in terahertz detection," Applied Physics Letters **115**, 211105 (2019).
[24] A. Rubano, S. Mou, L. Marrucci, and D. Paparo, "Terahertz Hyper-Raman Time-Domain Spectroscopy," ACS Photonics **6**, 1515–1523 (2019).
[25] A. Ceraso, S. Mou, A. Rubano, and D. Paparo, "Coherent THz Hyper-Raman: Spectroscopy and Application in THz Detection," Materials **12**, 3870 (2019).
[26] A. V. Ovchinnikov, O. V. Chefonov, E. D. Mishina, and M. B. Agranat, "Second harmonic generation in the bulk of silicon induced by an electric field of a high power terahertz pulse," Scientific Reports **9**, 9753 (2019).
[27] T.-J. Wang, J.-F. Daigle, S. Yuan, F. Théberge, M. Châteauneuf, J. Dubois, G. Roy, H. Zeng, and S. L. Chin, en"Remote generation of high-energy terahertz pulses from two-color femtosecond laser filamentation in air," Physical Review A **83**, 053801 (2011).
[28] A. D. Koulouklidis, C. Gollner, V. Shumakova, V. Y. Fedorov, A. Pugžlys, A. Baltuška, and S. Tzortzakis, en"Observation of extremely efficient terahertz generation from mid-infrared two-color laser filaments," Nature Communications **11**, 292 (2020).
[29] N. Karpowicz, J. Dai, X. Lu, Y. Chen, M. Yamaguchi, H. Zhao, X.-C. Zhang, L. Zhang, C. Zhang, M. Price-Gallagher, C. Fletcher, O. Mamer, A. Lesimple, and K. Johnson, en"Coherent heterodyne time-domain spectrometry covering the entire "terahertz gap"," Applied Physics Letters **92**, 011131 (2008).
[30] M. Stavola, "Infrared spectrum of interstitial oxygen in silicon," Applied Physics Letters **44**, 514–516 (1984).
[31] M. Lax and E. Burstein, "Infrared Lattice Absorption in Ionic and Homopolar Crystals," Physical Review **97**, 39–52 (1955).
[32] E. L. Shirley and H. M. Lawler, "Two-phonon infrared spectra of Si and Ge: Calculating and assigning features," Physical Review B **76**, 054116 (2007).
[33] J. J. Letcher, K. Kang, D. G. Cahill, and D. D. Dlott, "Effects of high carrier densities on phonon and carrier lifetimes in Si by time-resolved anti-Stokes Raman scattering," Applied Physics Letters **90**, 252104 (2007).
[34] F. Cerdeira and M. Cardona, "Effect of Carrier Concentration on the Raman Frequencies of Si and Ge," Physical Review B **5**, 1440–1454 (1972).
[35] F. A. Johnson, "Lattice Absorption Bands in Silicon," Proceedings of the Physical Society **73**, 265–272 (1959).
[36] M. Ikezawa and M. Ishigame, "Far-Infrared Absorption Due to the Two-Phonon Difference Process in Si," Journal of the Physical Society of Japan **50**, 3734–3738 (1981).
[37] S. K. Cushing, M. Zürch, P. M. Kraus, L. M. Carneiro, A. Lee, H.-T. Chang, C. J. Kaplan, and S. R. Leone, "Hot phonon and carrier relaxation in Si(100) determined by transient extreme ultraviolet spectroscopy," Structural Dynamics **5**, 054302 (2018).
[38] Y. R. Shen, *The principles of nonlinear optics* (J. Wiley, New York, 1984).

[39]Z. Han, S. A. Kivelson, and P. A. Volkov, "Quantum Bipolaron Superconductivity from Quadratic Electron-Phonon Coupling," Physical Review Letters **132**, 226001 (2024).
[40]X. Zhu, L. Santos, C. Howard, R. Sankar, F. C. Chou, C. Chamon, and M. El-Batanouny, "Electron-Phonon Coupling on the Surface of the Topological Insulator Bi 2 Se 3 Determined from Surface-Phonon Dispersion Measurements," Physical Review Letters **108**, 185501 (2012).
[41]A. K. Geim and I. V. Grigorieva, "Van der Waals heterostructures," Nature **499**, 419–425 (2013).